Lysozyme-sensitive plasmonic hydrogel nanocomposite for colorimetric dry-eye inflammation biosensing

Yasamin Ziai,[a] Chiara Rinoldi,[a] Francesca Petronella,[b] Anna Zakrzewska,[a] Luciano De Sio,[c] Filippo Pierini[a]*

Detection of lysozyme levels in ocular fluids is considered crucial for diagnosing and monitoring various health and eye conditions, including dry-eye syndrome. Hydrogel-based nanocomposites have been demonstrated to be one of the most promising platforms for fast and accurate sensing of different biomolecules. In this work, hydrogel, electrospun nanofibers, and plasmonic nanoparticles are combined to fabricate a sensitive and easy-to-use biosensor for lysozyme. Poly(L-lactide-co-caprolactone) (PLCL) nanofibers were covered with silver nanoplates (AgNPls), providing a stable plasmonic platform, where poly(N-isopropylacrylamide)-based (PNIPAAm) hydrogel layer allows mobility and well-integration of the biomolecules. By integrating these components, the platform can also exhibit a colorimetric response to the concentration of lysozyme, allowing for easy and non-invasive monitoring. Quantitative biosensing operates on the principle of localized surface plasmon resonance (LSPR) induced by plasmonic nanoparticles. Chemical, structural, thermal, and optical characterizations were performed on each platform layer, and the platform's ability to detect lysozyme at concentrations relevant to those found in tears of patients with dry-eye syndrome and other related diseases was investigated by colorimetry and UV-Vis spectroscopy. This biosensor's sensitivity and rapid response time, alongside the easy detection by the naked eye, make it a promising tool for early diagnosis and treatment monitoring of eye diseases.

Introduction

Lysozyme, an essential protein in various body fluids, plays a pivotal role in the body's innate immune defense against bacterial infections.[1] It has gained widespread recognition as a highly effective antibacterial agent, particularly renowned for its efficacy against Gram-positive bacteria due to ability to break down their cell walls.[2] Notably, c-type lysozyme exhibits presence in bodily fluids, with concentration reaching its peak in tears and serum, ranging from 1 to 2 $g.L^{-1}$,[3] while being present at lower levels, around 1 to 10 $\mu g.L^{-1}$, in urine and cerebrospinal fluid.[4] Detecting elevated or dropped lysozyme levels can serve as a valuable non-specific indicator for various diseases in pathological conditions. For instance, heightened lysozyme levels have been associated with AIDS,[5] leukemia,[6] and dry-eye disease (DED).[7] As a result, monitoring lysozyme as a biomarker provides essential insights to track patients' health status and make well-informed decisions regarding diagnosis, treatment, and disease progression.

Consequently, the escalating demand for affordable, rapid, and user-friendly biosensors enabling point-of-care diagnostics has led to developments in biosensing. Among the various affinity biosensors, those utilizing plasmonic materials have attracted significant attention due to their potential for studying surface plasmon resonance (SPR) signals resulting from lysozyme binding to receptors.[8] Plasmonic materials, notably noble metals like gold and silver, display an intriguing optical phenomenon when light excites from interactions between incident light and surface electrons, manifesting as an extinction spectrum.[9] Moving towards nanotechnology, noble nanoparticles have substantially enhanced biosensor sensitivity, enabling the detection of low concentrations of biomarkers and small biomolecules.[10,11] The optical properties of plasmonic materials, specifically the refractive index (RI) and resonance wavelength (λ_{max}), can be precisely controlled by manipulating factors such as nanoparticle shape, size, interparticle spacing, and the immediate surrounding environment. These attributes offer versatility across a broad spectral range, affording flexibility in designing biosensors for diverse applications.[12]

Additionally, the ability to tailor the receptor environment further enhances the adaptability of plasmonic biosensors to varying matrices.[13,14] In conjunction with the precise localized surface plasmon resonance (LSPR) biosensing methods, incorporating visual aids for rapid result determination can prove highly advantageous within practical applications. Visual colorimetry technique facilitates the rapid assessment of biomarker alterations resulting from nanoparticle aggregation.[15] Using the unique properties of plasmonic nanoparticles, a color change can be detected upon binding biomolecules to the surface of the nanoparticles. This phenomenon alters the absorption wavelength and scatter light. The intensity of the shift and color change can be directly correlated with the concentration of the target biomarker, offering a rapid and straightforward means of analysis[16,17]

Li *et al.* used a hybrid system comprising gold nanoparticles and ruthenate to detect lysozyme. In the absence of lysozyme, introducing ruthenate leads to particle aggregation, resulting in a visible color shift from red to blue. Conversely, in the presence of lysozyme, an electrostatic charge alteration induced by the interaction between plasmonic particles and ruthenate prevents aggregation, thereby preserving the original coloration.[18] A similar approach was undertaken by Castillo *et*

al., who employed sodium chloride (NaCl) for lysozyme detection in urine samples. In this study, they harnessed the potential of particle aggregation, both in the presence and absence of lysozyme, as induced by NaCl.[19]

A suitable platform to carry the nanoparticles and provide a proper detecting matrix is necessary to maximize detection efficiency. Nanofibers, fabricated using the electrospinning technique, are promising candidates as substrates to carry plasmonic nanoparticles. Electrospinning involves applying an electric field to a polymer solution or melt, causing the polymer to elongate into ultrafine fibers with diameters ranging from nanometers to micrometers. This unique method enables the production of nanofibers with exceptional structural characteristics, including a high aspect ratio and interconnected porous network, alongside tunable mechanical properties.[20] Electrospun nanofibers from various natural and synthetic polymers have been widely used in biomedical applications such as tissue engineering,[21] wound dressing,[22] drug delivery,[23] and biosensing.[24] Upon applying noble metal nanoparticles like gold or silver, the nanofibers can serve as ideal hosts for these nanoscale components due to their abundant surface area, enabling a higher loading capacity of plasmonic materials.[25] From another point of view, focusing on enhancing the transport and detection of biomolecules and biomarkers within biosensing platforms, hydrogels have appeared as a promising class of materials, serving as carriers for these tiny particles such as nanofillers and biomarkers.[26]

Hydrogels, characterized by their three-dimensional network structures, retain substantial amounts of water within their matrix. The high water capacity of hydrogels facilitates the efficient and controlled transport of biomolecules and biomarkers, allowing for enhanced interactions and improved sensitivity in biosensing assays. Their tunable and biocompatible nature further augments their suitability for accommodating diverse biomolecules and their feasibility for specific needs.[27] Stimuli-responsive hydrogels exhibit reversible physical changes in response to minor alterations in their surrounding environment which helps in terms of reusability of the final product. Among these, poly(N-isopropylacrylamide)-based hydrogels stand out as a class of smart hydrogels with thermo-responsive behavior.[28] Incorporating recognition elements in the hydrogel structure allows for responsive reactions with specific chemical substances.

Consequently, these interactions trigger changes in the solubility or charge state of the hydrogel. Likewise, solubility changes can directly influence the hydrogel's volume response.[29] Notably, these smart hydrogels demonstrate remarkable volume variations in response to even minor temperature fluctuations, making them particularly well-suited for various applications where precise temperature responsiveness is desirable.[30]

Here in this research, we have fabricated a composite platform consisting of poly(L-lactide/ε-caprolactone) (PLCL) nanofibers, silver nanoplates (AgNPls), and PNIPAAm hydrogel as a biosensor for lysozyme enzyme. AgNPls were drop-casted onto the electrospun mat to provide a stable layer for detection, followed by the addition of hydrogel precursor. Penetration of the hydrogel into the structure of the mat before polymerization allows for the biomarkers to maneuver, resulting in facile recognition and efficient sensing. Each composite material component was investigated individually, and subsequently, an analysis of the entire composite was performed as a unified entity. A rapid colorimetry assay based on the aggregation of AgNPls was also tested to check the system's applicability for naked-eye lysozyme detection. Photothermal responses and the sensing limits were examined, demonstrating the material's potential suitability as a viable candidate biosensor for lysozyme detection.

Materials and methods

Materials

N,N-isopropylacrylamide (NIPAAm, 97%, Sigma Aldrich, Poland), N-isopropylomethacrylamide (NIPMAAm, 97%, Sigma Aldrich, Poland), N,N'-methylene bisacrylamide (BIS-AAm, 99.5%, Sigma Aldrich, Poland), 2-Hydroxy-4'-(2-hydroxyethoxy)-2-methylpropiophenone (Irgacure 2959, 98%, Sigma Aldrich, Poland), silver nanoplates (AgNPls, 53 nm, PVP, Nanocomposix, USA), Poly (L-lactide/ε-caprolactone) (PLCL 70/30, Mn 80 kDa, Sigma Aldrich, Poland), Chloroform ($CHCl_3$, POCh, Poland), N,N-dimethylformamide (DMF, POCh, Poland), Lysozyme human (≥100,000 units mg^{-1} protein, Sigma Aldrich, Poland), and Sodium chloride (NaCl, ≥99%, Sigma Aldrich, Poland) were used as received.

Electrospinning of PLCL

10% (w/w) of PLCL was dissolved into a chloroform/DMF solution mixture with a 90:10 (w/w) ratio. The solution was kept on stirring overnight using a magnetic stirrer prior to the electrospinning process. The electrospinning process was optimized to use a 15 kV positive voltage, 800 µL h^{-1} flow rate, and a 26G needle tip at a distance of 15 cm from a rotating drum collector with 500 rpm speed to achieve favorable fibers. Electrospun nanofibers in the shape of a mat were collected after using 2 mL of solution to achieve convenient thickness at room temperature (25 °C) and 40% relative humidity.

Hydrogel precursor sol

A mixture of 578.13 mg NIPAAm, 15.63 mg NIPMAAm, 31.25 mg BIS-AAm, and 12.5 mg Irgacure 2959 was prepared. This mixture was dissolved in 10 mL of deionized water to reach 95.2 wt% of the solution. The sol was protected from light while stirred overnight using a magnetic stirrer up to its complete dissolution.[24]

Fabrication of the nanostructured platform

First, an aqueous solution of AgNPls with 6.5% (v/v) was added onto the mat's surface via the drop-casting method to fabricate the nanocomposite structure. Kept under the hood, the water evaporated, and a composite of PLCL nanofibers loaded with AgNPls was ready to use. Mats were cut in the favored size and shape and placed in the same shape mold, where hydrogel sol was added to the top. It is worth mentioning that argon

bubbling must be applied to the sol before use to remove any oxygen in the mixture. The mold was placed in an ice bath and irradiated by an ultra-violet (UV) lamp (Dymax lamp with 400 W capacity and a power density of 225 mW cm^{-2}) for 90 seconds.

Structural characterization

Field emission scanning electron microscopy (FE-SEM) and scanning electron microscopy (SEM) were performed with ZEISS Crossbeam 350 and JSM-6010PLUS/LV microscopes, respectively. Hydrogel discs and the final construct were both firstly frozen in liquid nitrogen before cutting the cross-section to ensure a sharp cut, and then freeze-driedusing a lyophilizer (Labconco FreeZone). Before imaging, samples were sputtered with gold layers around 8 nm thick using a II-29030SCTR JEOL Smart Coater. The lyophilized materials were cut into small pieces, immersed in ethanol, and placed on a copper mesh with an amorphous carbon membrane. The size of nanofibers and hydrogel pores was then calculated using ImageJ. For transmission electron microscopy (TEM), samples were analyzed on an FEI Talos F200X TEM (acceleration voltage of 200 kV) after four hours of drying in a vacuum drier.

Energy-dispersive X-ray spectroscopy (EDX) analysis was also conducted using scanning transmission electron microscopy (STEM). This involved using a high-angle annular dark-field detector and a Super-X EDX system equipped with four silicon drift detectors (SDDs). The topography of the sample surface was examined using an atomic force microscope (AFM, Ntegra, NT-MDT) that featured a silicon cantilever (NSG01, NT-MDT, tip radius 10 nm). These AFM measurements were carried out in semi-contact mode at a resonance frequency of 150 kHz, capturing 500x500 data points per image. The hydrodynamic size of the AgNPls was determined through dynamic light scattering (DLS) using a Zetasizer Nano ZS analyser (Malvern Instruments). Aqueous dispersions containing 0.1% wt of AgNPls were prepared, and the samples were placed into quartz micro-cuvettes for triple measurements to establish an average size value. DLS was performed before and after sonication (500 W, 20 kHz, 3 min; Vibra-Cell™ Ultrasonic Liquid Processor).

Chemical characterization

A Multiskan GO spectrophotometer (Thermo Scientific, USA) was used to collect data on ultraviolet-visible (UV-Vis) spectra. UV-Vis spectrophotometer scanned from 400 nm to 1000 nm every 5 nm. Fourier-transform infrared (FT-IR) spectroscopy was used to characterize the functional groups in each layer. FT-IR analyses were conducted in an attenuated total reflectance (ATR) mode with a Bruker Vertex70 FT-IR Spectrometer and carried out in the wavenumber range of 4000-400 cm^{-1} with a resolution of 2 cm^{-1} and eight scans for each sample. Using an OCA 15EC goniometer and droplets of 1 µl, contact angle meauserments were conducted and the average contact angle was calculated using ImageJ.

Photothermal-responsivity characterization

The near-infrared (NIR) light source utilized was a diode laser from CNI (Changchun New Industries Optoelectronics Technology Co., Ltd.), which operates within the absorption spectrum of AgNPls (longitudinal plasmon band) and features a rectangular beam profile. To assess and visualize the spatial distribution of heat and the temperature profile during a 300-seconds laser exposure, a high-resolution thermal camera (FLIR, A655sc) was used. This camera captures thermal images at a resolution of 640x480 pixels with a precision of ±0.2 °C. Additionally, it integrates smoothly with the FLIR ResearchIR Max software, which handles and analyzes the collected thermal data.

Colorimetry

Visual colorimetric analysis was conducted on optimized solutions, considering the lysozyme concentration in a single eye drop, AgNPls concentration, and the utilization of commercially available 0.9% sodium chloride solution serum, commonly known as saline solution. Various concentrations of lysozyme and AgNPls mixtures were prepared, and each solution was subsequently augmented with saline solution. The alteration in coloration was documented using a standard smartphone camera, both before and after the addition of NaCl, with intermediate recordings captured at 10, 30, and 60-minute intervals. Simultaneously, a Multiskan GO spectrophotometer (Thermo Scientific, USA) was employed to record changes in the absorption spectra of each sample at the same time intervals.

For the colorimetric analysis of the finalized platform, pre-fabricated platforms were air-dried and subsequently immersed in a lysozyme solution, allowing the hydrogel component of the platform to swell to its original dimensions for 2 hours. Following this, saline solution was introduced into the platform, with observable color changes manifesting within 15 minutes.

Lysozyme sensing tests

The absorption spectra of AgNPls-based platforms were collected by using a UV-Vis spectrometer (Lambda 365, Perkin Elmer). The sensing ability of the AgNPls-based platforms was tested by preparing standard solutions of lysozyme in milli-Q water at the following concentrations: 2 mg mL^{-1}, 1.5 mg mL^{-1}, 1 mg mL^{-1}, and 0.5 mg mL^{-1}.

The samples were placed on a glass substrate, and then 200 µL of each lysozyme standard solutions was cast on the respective AgNPls-based platform to induce the penetration of the solution. The AgNPls-based platforms were kept at rest for 15 minutes in the dark to promote a uniform and complete distribution of the solutions within the samples before evaluating the optical response.

At this stage, the excess of the lysozyme solution (not in direct contact with the sample) was delicately removed, and each wet nanoplatform was carefully placed in the sample holder to measure its absorption spectrum.

Each absorption spectrum was mathematically converted into its first-order derivative to determine the wavelength of the plasmon peak of AgNPls (λ_{max}).
After that, the optical shift (Δλ) was calculated as the difference between the λ_{max} value measured after (λ_{max_lyso}) and before (λ_{max}) the contact with the lysozyme solution, respectively (Equation 1).

$$\Delta\lambda = \lambda_{max} - \lambda_{\max\ \_lyso} \quad (1)$$

The Δλ values (three replicate for each experimental points were plotted as a function of the respective lysozyme concentration to obtain the calibration curve, and the experimental points were interpolated using a linear fit.
The sensing limits was evaluatedas three times the standard deviation of the blank.
In particular, the AgNPls-based platform was analyzed by the absorption spectroscopy. Then, It was cast with 200 µL of milli-Q water, and the absorption spectrum was measured again. Each absorption spectrum was mathematically converted into its first-order derivative to determine the wavelength of the plasmon peak of AgNPls (λmax), and the Δλ value. This procedure was replicated five times, to calculate the standard deviation of the average Δλ value. The resulting standard deviation was multiplied by three and associated with the lysozyme concentration based on the calibration curve, thus determining the sensing limit of the system.
The AgNPls-based platforms were also tested for the direct detection of lysozyme in a sample of human tears. First, the absorption spectrum of an AgNPls-based platform was measured and converted in its first derivative. At this point a sample of tears was obtained from a donor who has been wearing contact lenses for 5 hours without using any moisturizing or wetting solution. The lenses were removed, and tearing was then further stimulated by gently rubbing the eye area. At this point, the tears were collected in 200 µL eppendorf tubes. The entire content of the eppendorf tubes (approximatively 150 µL) was then deposited on the an AgNPls-based platform previously placed on a glass support. The excess of the liquid was gently removed and the system was let to rest for 15 minutes in the dark to promote the complete penetration of the liquid inside the AgNPls-based platform. Finally the absorption of spectrum was collected and converted into its first derivative to determine the Δλ and measure the lysozyme concentration, based on the calibration curve.

Results and discussion

Silver nanoparticles (AgNPls)

AgNPls were selected as the plasmonic entities in this experimental platform with an average dimension of 40 ± 15 nm. The dimension specified here refers to an average, as the particles, despite having consistent sizes, exhibit various shapes such as triangular, circular and polygonal. The choice of these particular particles is strategic; The optical properties of nanoparticles are influenced by their shape and size. Even though these particles are of uniform size, the presence of diverse shapes with sharp and round edges enhances the precision and sensitivity of the biosensor.[31] The morphological diversity of platelet-shaped AgNPls is precisely captured through TEM images in **Figure 1a-c**, each offering a different shape and controlled thickness. DLS measurements were conducted on the nanoparticles before and after sonication. The nanoparticles' average size was also calculated using DLS, where they are reported to be an average of 57.2 ± 0.53 nm. Although the difference between the size resulted from the TEM and DLS method due to the hydrodynamic radius is a known fact, having different shapes of the nanoplates offering a more diverse hydrodynamic radius has its effect in this case. The observation that their average size remained consistent throughout sonication is additional evidence of their stability and resistance to aggregation (**Figure S1, S2**). An example of representative particle dispersion is also visually presented in the TEM image in **Figure 1d**, confirming the stability of nanoparticles and the absence of inter-particle aggregation phenomena.
Further insight into the features of these nanoparticles is offered by EDS elemental mapping, as shown in **Figure 1e**, highlighting the structural shape of the nanoparticles with the average size and distribution. Morphological characterization continues via FE-SEM visualization, as shown in **Figure 1f**, showing a comprehensive understanding of the plasmonic nanoparticles' topographical dispersion. As can be seen, AgNPls are well-distributed, and there are no signs of aggregation between them, confirming their stability in the system.

Fabrication of multi-layer nanostructured platform

The stepwise procedure of fabrication of the final nanostructure is illustrated in **Figure 2a**. In the initial step, the electrospinning technique was used to fabricate the PLCL nanofibrous mat. Several critical parameters, including voltage, flow rate, working distance, and needle gauge size, were optimized to attain the desired uniform nanofibers. The nanofibrous mat was subsequently sectioned into well-plate dimensions using a cork borer. In each well, precise aliquots of AgNPls with a defined concentration of 65 µL mL^{-1} were introduced with a drop-casting methodology. The well plate was then sealed and incubated overnight in darkness to facilitate particle deposition within the network as the solvent gradually evaporated. Notably, a visible visual transition, from white to blue, was observed upon AgNPls introduction, confirming their presence within the system. A solution of hydrogel precursor, prepared as outlined in the materials and methods section, was then added to the plasmonic nanofibers. This solution incorporated NIPAAm and NIPMAAm monomers along with Irgacure as a photoinitiator, necessitating UV irradiation to initiate photo-polymerization. Before polymerization, the precursor solution underwent a brief period of argon bubbling to deplete oxygen content effectively. Subsequently, the precursor solution was uniformly dispensed onto each plasmonic nanofiber within the well plate. The entire assembly was carefully immersed in an ice bath when UV irradiation was applied for 60 seconds to complete the hydrogel polymerization process. Utilizing an ice bath is imperative so that the temperature does not exceed the

characteristic lower critical solution temperature (LCST) during UV irradiation. Each part of the platform was characterized separately.

Material characterization involved AFM topographic analysis of PLCL fibers is presented in **Figures 2b, c**. These images provide an illustrative representation of the surface topography of the fibers, offering insights into their size and morphology. Figures 2a and 2b, with 5 µm and 2.5 µm Z-scale bars, respectively, represent the vertical changes in cantilever position over the sample. This Z-scale, denoting sensor height topography, is an indicator of surface properties. As can be seen, AFM images were also done after particle drop-casting. However, as a result of the size and well-dispersion of the particles, no sign of the particles was seen in the AFM images regarding the magnification. FT-IR spectroscopy, as depicted in **Figure S3**, shows the chemical composition of nanofibers with and without AgNPls. Notably, there is no sign of the silver content within the electrospun fiber network in the detection range of the experiment which is a sign of no aggregation of the nanoparticles and their stability in the system.

Remarkably, a transition in wettability features is detected through contact angle measurements (**Figure 2d, e**). Specifically, the contact angle of the fibers is dropped from 128.8° to 71.3°, indicating a shift from hydrophobicity to hydrophilicity. This can happen due to changes in the surface charge and energy of the mat which is also known as nanoparticle-induced hydrophilicity.[32] This alteration in surface characteristics is of great significance, particularly concerning following fabrication steps involving adding a hydrogel precursor solution composed mainly of aqueous content. The increased hydrophilicity of the fibers facilitates solution permeation throughout the fibrous network, thereby fostering superior integration, anchorage efficacy, and consequent structural stability within the final platform.[33] As shown in the FE-SEM image in **Figure 2f**, nanofibers are in the same shape and diameter, uniform and continuous with an average diameter of 1.478 ± 0.183 µm. **Figure 2g** shows the interconnected porous 3D structure of hydrogel, where the pore sizes have a 2-5 µm dimension. This image has been taken from pure hydrogel prepared separately after freeze-drying to show precisely the intra-structure of the hydrogel. Finally, **Figures 2h** and **2i** show the crosssection between the hydrogel and fiber layers and their anchorage and penetration. These images confirm the hydrogel's stable structure and full fiber penetration. This platform feature helps the following application regarding biosensing of lysozyme, as it allows biomolecule transition into the network, offering more sensing area.

Fast photothermal responsiveness of the nanocomposite

The NIR-induced photothermal-responsive characteristics of the plasmonic nanoplatforms were explored using a red laser operating at 808 nm wavelength with an intensity of 1500 mW cm^{-2}. The presence of AgNPls within the platform is a distinctive absorption peak within the visible spectrum, showing exceptional photothermal efficiency by converting absorbed light into thermal energy. As the generated heat from the NIR laser, operating at the absorption peak surpasses the hydrogel's volume phase transition temperature (VPTT), a cascade-like series of stimulus-response events happen, resulting in a shrinkage of the hydrogel and subsequent expulsion of water. These phenomena are the significant thermo-responsive properties inherent to the hydrogel.

Figure 3a illustrates the experimental setup used for the photothermal assessment of the composite platform. A continuous-wave (CW) laser source emits an 808 nm wavelength laser beam, which irradiates upon the composite platform following passage through a custom-designed optical apparatus. Thermographic imaging, capturing variations in sample temperature throughout different irradiation durations, is recorded by a thermal camera positioned orthogonally to the sample.

In **Figure 3b**, thermal images corresponding to various hydration levels and irradiation durations of the platform are presented. Employing thermal imaging technology, we observed an immediate temperature elevation in both dry and hydrated states of the platform, indicating a direct responsiveness to the applied stimuli. Testing in both conditions gave us an understanding of the capability of the system to perform under different conditions, for further investigations towards final goal of biosensing. Notably, compared to pure NIPAAm-based hydrogels lacking photothermal responsiveness, the introduction of plasmonic AgNPls modifies the composite into a highly photothermal-responsive platform. Dry samples exposed to laser irradiation for 300 seconds exhibited a temperature rise to approximately 48 °C, while under identical conditions, hydrated platforms reached a maximum temperature of 39.7 °C. This disparity arises from variations in the absorption peak between hydrated and dry states, causing a shift in the absorption profile when in a fully hydrated state, no longer optimally aligned with laser emissions, thus reducing photoresponsivity. This phenomenon can also be attributed to differences in the surrounding media; Notably, considering the immediate vicinity of the plasmonic particles, water has higher thermal capacity, leading to minor changes in temperature. These findings are presented as time-temperature profiles in **Figure 3c**. While the laser remained active, prompt temperature elevations of nearly 50 °C in the dry state and up to 40 °C in the hydrated state were evident. In both scenarios, the temperature escalation can be attributed to the photothermal efficiency of AgNPls. Following the deactivation of the laser and removing the pump beam, the samples swiftly returned to room temperature, taking less than one minute. This property can be beneficial in the reusability of the nanoplatforms, allowing them to be easily washed with just hot water and changes in volume, thereby enabling their repeated use.

Visual colorimetry

Using NaCl as an aggregating agent, visual colorimetry was employed in both the solutions and the final platform. Following the methods detailed earlier, we conducted visual colorimetry on previously optimized solutions comprising plasmonic particles, lysozyme, and saline. Given that a healthy lysozyme concentration typically falls between 1-2 mg mL^{-1}, with levels

under 1 mg mL^{-1} considered indicative of unhealthy conditions, we chose to test various lysozyme concentrations of 0, 0.5, 1, 1.5, and 2 mg mL^{-1}. **Figure 4a** shows the schematic of the principle behind colorimetry using NaCl as a salt. The system containing the same amount of silver is exposed to various concentrations of lysozyme, ranging from unhealthy to healthy. Upon adding the lysozyme to the system, the biomolecule tends to attach to the surface of the nanoparticles. Visual colorimetry happens when using a standard concentration of NaCl available in saline serum. By infiltrating the platforms with the saline solution, due to the changes in the surface charges of nanoparticles, they tend to aggregate. In the healthy range of lysozyme presence, they will act as shields and do not let the aggregation occur, whereas, in the non-sufficient amount of lysozyme, they can not defeat NaCl. This will result in the aggregation of nanoparticles, which will appear as a change in absorbance peak and visual color. **Figures 4b** and **4c** depict the absorption spectra of the samples immediately after NaCl addition and after 60 minutes. The peak wavelengths initially showed subtle shifts, indicating limited particle aggregation, particularly in samples 2 and 5. However, after 60 minutes, as shown in Figure 4c, more significant shifts in absorption wavelengths were evident, leading to visible color changes.

Changes in the absorption spectra of the solution were measured using UV-Vis spectrometer at other time points like 10 and 30 minutes (**Figure S4, S5**). Using these data, **Figure S6** presents the correlation between lysozyme concentration and changes in maximum absorption wavelengths, revealing a linear trend. This underscores that in our optimized system, higher lysozyme concentrations yield smaller Δλ values, resulting in more stable color shades compared to the prominent color changes observed at lower concentrations, as illustrated in Figure S6. **Figure 4d** demonstrates the result of NaCl addition at four different time points. Initially, when lysozyme was added to the aqueous AgNPls solution, all samples exhibited the same blue coloration. However, upon the addition of the designated amount of NaCl, noticeable color changes were observed. Samples 1 and 2, representing lysozyme concentrations below the healthy range, exhibited a rapid shift to a more purple hue. Over time, these color changes became even more pronounced at the 30 and 60-minute intervals, while samples 4 and 5, containing healthy lysozyme levels, remained stable. This reaffirms the viability of our method for visual colorimetry. The changes in the wavelength Δλ were also described in a bar chart provided in **Figure 4e**. As seen in this demonstration, samples below the healthy region underwent enormous Δλ; In contrast, those with a healthy amount of lysozyme stayed in the same wavelength region with minimal change.

Moreover, we extended our investigations to assess potential color changes on the final platform. It is noteworthy that due to the extended travel time of particles within the porous hydrogel structure, it takes more time for color changes to become apparent. After applying the requisite amount of lysozyme and NaCl as specified in the methods section, we observed a visible color change in the sample with 0.5 mg mL^{-1} of lysozyme, indicating the potential practicality of the platform (**Figure S7**).

Lysozyme biosensing

The absorption spectrum of the Ag nanoplates-based platform is reported in **Figure 5a** (Blue curve). The spectrum shows an increasing absorption internsity in the range from 500 nm to 1000 nm, with a shoulder appearing at 540 nm. To better identify this absorption signal, the spectrum was converted to its first derivative, as depicted in the red line of Figure 5a. By differentiating the spectrum, we can appreciate the rate of absorbance change as a function of the wavelength. It allows the identification of minor spectral features, removing the effects of the matrix and the background.[34] Indeed, the first derivative absorption spectrum points out an absorption deep at 540 nm. This absorption signal can be safely associated with the plasmon band of AgNPls, and the broad peak indicates the effect of different shapes of the nanoparticles, where they have the same size. The position of the AgNPls plasmon band is blue-shifted with respect to the maximum of the plasmon band of Ag nanoplates dispersed in water due to the variation of the refractive index of the medium.[34]

Experimental results reported in **Figure 5b** highlight the spectroscopic behavior of the Ag-based nanoplatforms as a function of the surrounding refractive index. The sample showed an absorption deep at 605 nm; However, when it is soaked with pure water or lysozyme, the deep shifts to 557 nm and 534 nm, respectively. The spectral blue shift of the absorption spectrum can be ascribed to a variation in the refractive index surrounding Ag nanoplates. After the milli-Q water is introduced into the dried sample, the average refractive index is expected to decrease slightly, probably due to the alteration of the density of polymer molecules. Accordingly, the decreased local refractive index value resulted in a blue shift of 48 nm of the plasmon bands of AgNPls. Also, the introduction of lysozyme solution determined a 71 nm-blueshift of the Ag nanoplates plasmon band. The sensitivity of the plasmon wavelength position is exploited to use the AgNPls-based platforms as a biosensing system for lysozyme quantification.

To investigate the possibility of detecting the lysozyme from bodily fluids, we have first to assess the potential and limit of detection of the nanoplatforms. The AgNPls-based samples were soaked with solutions with different concentrations of lysozyme ranging from 0 mg mL^{-1} to 2.5 mg mL^{-1}. The absorption spectrum is collected and mathematically converted in its first derivative to measure the λ_{max}. At this stage, the Δλ is calculated with Equation 1 and reported as a function of the lysozyme concentration (**Figure 5c**) resulting in a linear correlation. The Δλ linearly decrease as a function of of the lysozyme concentration. This behaviour can be associated with a progressive decrease in the refractive index index experienced by the AgNPls that is affected by the polymeric matrix and by the infiltrating medium, as observed in paper previously reported.[24]

The next set of experiments was conducted to examine the possibility of nanoplatforms being used to detect the human eye's tears and the amount of lysozyme. **Figure 5d** shows the experiment's procedure, starting with collecting tears from a normal eye. The AgNPls-based nanoplatform, placed on a glass

support, was infiltrated with the tear sample, and after 15 min required for the complete platform infiltration the absorption spectrum was measured and converted in its first derivative to carefully determine the Δλ. **Figure 5e** shows the results of this experiment. Analysis of the experimental data using tears revealed a blue shift of 26 nm. Based on the linear interpolation in Figure 5c, this shift corresponds to a lysozyme concentration of 3.6 mg mL^{-1}. The donor wore contact lenses for over 5 hours and stimulated lacrimation. This elevated concentration suggests a potential inflammatory state, which can be detected using the developed AgNPls-based nanoplatform.

Conclusions

In this work, we have successfully designed and fabricated a soft nanocomposite platform by integrating PLCL nanofibers covered with AgNPls and a PNIPAAm hydrogel for biosensing application. PLCL nanofibers with high surface area provide physical stability to the system and, with their unique structural properties, provide a stable substrate to carry nanoparticles. Silver nanoplates, a type of plasmonic nanoparticle, were added to the system with the aim of colorimetry and LSPR biosensing of lysozyme. A NIPAAm-based hydrogel layer was added to the system to offer a more available matrix for the final purpose of the nanoplatform. Hydrogels, with their high water content, will provide a transportable matrix for nanoparticles and biomolecules, making biosensing efficient and sensitive. The design of AgNPls-based nanoplatform represents a significant advancement in the non-invasive and efficient detection of lysozyme levels in ocular fluids. Comprehensive chemical, optical, and structural characterization of layers of nanoplatform was conducted, ensuring a well-fabricated and stable platform. Photothermal characterization of the platform using a thermal camera confirms the possibility of reusability of the system, benefiting from the synergy effect of NIPAAm-based hydrogel and AgNPls. The possibility of visual colorimetry was tested on the system, showing the color change from blue to purple hue in the case of dry-eye condition. The innovative approach of colorimetry using saline serum, available to everyone, makes this system an accessible and non-invasive method for examining their health. The LSPR phenomenon induced by plasmonic nanoparticles was done to make the biosensing more quantitative and underscore its capability to accurately detect lysozyme concentrations in conditions such as dry-eye syndrome. The biosensor's notable sensitivity, rapid response time, and simplicity of visual detection reveal its potential as a valuable tool for the early diagnosis and ongoing management of various eye-related health issues.

Author Contributions

Y.Z. designed the experiments and fabricated the nanoplatforms. Y.Z. performed the morphological and chemical characterization of nanofibers. A.Z. performed FE-SEM and TEM analyses. Y.Z. and C.R. performed the colorimetry experiments. F.Pe and L.D. performed the biosensing experiments with human tears. Y.Z. wrote the manuscript. F.Pi. conceived the idea and supervised the project. All authors discussed the results and commented on the manuscript.

Conflicts of interest

There are no conflicts to declare.

Acknowledgments

This work was supported by the National Science Centre (NCN) SONATA BIS Project No. 2020/38/E/ST5/00456. Figures 2, 3, 4, and 5 were partially created with BioRender. C.R. and F.Pi. acknowledge the financial support from the Polish Ministry of Science and Higher Education through scholarships for outstanding young scientists.

References

1 T. Jesse Joel, S. Suguna S. and S. R. Steffi, *Asian J. Pharm. Res. Heal. Care*, 2016, **8**, 42–46.

2 G. Leśnierowski and T. Yang, *Trends Food Sci. Technol.*, 2021, **107**, 333–342.

3 R. L. Pietsch and M. E. Pearlman, *Arch. Ophthalmol.*, 1973, **90**, 94–96.

4 J. Hankiewicz and E. Swierczek, *Clin. Chim. Acta*, 1974, **57**, 205–209.

5 M. H. Grieco, M. M. Reddy, H. B. Kothari, M. Lange, E. Buimovici-Klein and D. William, *Clin. Immunol. Immunopathol.*, 1984, **32**, 174–184.

6 P. Venge, T. Foucard, J. Henriksen, L. Håkansson and A. Kreuger, *Clin. Chim. Acta*, 1984, **136**, 121–130.

7 Z. Jia, W. Wei, K. Tu, B. Fang, M. Zhang and L. Shi, *Sensors Actuators B Chem.*, 2023, **378**, 133179.

8 G. Melinte, G. Selvolini, C. Cristea and G. Marrazza, *Talanta*, 2021, **226**, 122169.

9 Y. Ziai, C. Rinoldi, P. Nakielski, L. De Sio and F. Pierini, *Curr. Opin. Biomed. Eng.*

10 T. Špringer, M. L. Ermini, B. Špačková, J. Jabloňků and J. Homola, *Anal. Chem.*, 2014, **86**, 10350–10356.

11 F. Petronella, D. De Biase, … F. Z.-E. and undefined 2022, *pubs.rsc.orgF Petronella, D Biase, F Zaccagnini, V Verrina, SI Lim, KU Jeong, S Miglietta, V PetrozzaEnvironmental Sci. Nano, 2022•pubs.rsc.org*.

12 D. Stoia, L. De Sio, F. Petronella and M. Focsan, *Biosens. Bioelectron.*, 2024, **255**, 116243.

13 T. Xu and Z. Geng, *Biosens. Bioelectron.*, 2021, **174**, 112850.

14 M. Cottat, N. Thioune, A. M. Gabudean, N. Lidgi-Guigui, M. Focsan, S. Astilean and M. Lamy de la Chapelle, *Plasmonics*, 2013, **8**, 699–704.

15 X. Wang, Y. Xu, Y. Chen, L. Li, F. Liu and N. Li, *Anal. Bioanal. Chem.*, 2011, **400**, 2085–2091.

16 M. S. Verma, J. L. Rogowski, L. Jones and F. X. Gu, *Biotechnol. Adv.*, 2015, **33**, 666–680.

17 Y. Song, W. Wei, X. Qu, Y. Song, W. Wei and X. Qu, *Adv.*

Mater., 2011, **23**, 4215–4236.
18 J. Li, X. Mu, K. C. Chan, C. C. Ko and M. J. Li, *Microchim. Acta*, 2018, **185**, 1–6.
19 P. M. Castillo, F. J. Fernández-Acejo, J. M. Carnerero, R. Prado-Gotor and A. Jimenez-Ruiz, *Nanomater. 2021, Vol. 11, Page 612*, 2021, **11**, 612.
20 P. Nakielski, C. Rinoldi, M. Pruchniewski, S. Pawłowska, M. Gazińska, B. Strojny, D. Rybak, K. Jezierska-Woźniak, O. Urbanek, P. Denis, E. Sinderewicz, W. Czelejewska, J. Staszkiewicz-Chodor, M. Grodzik, Y. Ziai, M. Barczewska, W. Maksymowicz and F. Pierini, *Small*, 2022, **18**, 2104971.
21 C. Rinoldi, A. Fallahi, I. K. Yazdi, J. Campos Paras, E. Kijeńska-Gawrońska, G. Trujillo-De Santiago, A. Tuoheti, D. Demarchi, N. Annabi, A. Khademhosseini, W. Swieszkowski and A. Tamayol, *ACS Biomater. Sci. Eng.*, 2019, **5**, 2953–2964.
22 D. Rybak, Y. C. Su, Y. Li, B. Ding, X. Lv, Z. Li, Y. C. Yeh, P. Nakielski, C. Rinoldi, F. Pierini and J. M. Dodda, *Nanoscale*, 2023, **15**, 8044–8083.
23 K. Goodarzi, F. Jonidi Shariatzadeh, A. Solouk, S. Akbari and H. Mirzadeh, *Eur. Polym. J.*, 2020, **139**, 109992.
24 Y. Ziai, F. Petronella, C. Rinoldi, P. Nakielski, A. Zakrzewska, T. A. Kowalewski, W. Augustyniak, X. Li, A. Calogero, I. Sabała, B. Ding, L. De Sio and F. Pierini, *NPG Asia Mater.*
25 C. Cleeton, A. Keirouz, X. Chen and N. Radacsi, *ACS Biomater. Sci. Eng.*, 2019, **5**, 4183–4205.
26 H. R. Culver, J. R. Clegg and N. A. Peppas, *Acc. Chem. Res.*, 2017, **50**, 170–178.
27 Y. Ziai, C. Rinoldi, P. Nakielski, L. De Sio and F. Pierini, *Curr. Opin. Biomed. Eng.*, 2022, **24**, 100413.
28 G. Li, L. Zhang, Q. Han, T. Zheng, L. Wu, W. Guan, S. Sun and Y. Yang, *Compos. Part B Eng.*, 2023, **254**, 110551.
29 N. Sood, A. Bhardwaj, S. Mehta and A. Mehta, *Drug Deliv.*, 2016, **23**, 758–780.
30 S. Pawłowska, C. Rinoldi, P. Nakielski, Y. Ziai, O. Urbanek, X. Li, A. Kowalewski, B. Ding and F. Pierini, *Wiley Online Libr. Pawłowska, C Rinoldi, P Nakielski, Y Ziai, O Urbanek, X Li, TA Kowalewski, B DingAdvanced Mater. Interfaces, 2020•Wiley Online Libr.*
31 M. Shabaninezhad and G. Ramakrishna, *J. Chem. Phys.*, 2019, **150**, 144116.
32 N. Gao, Y. Yan, X. Chen and D. J. Mee, *Langmuir*, 2012, **28**, 12256–12265.
33 Y. Ziai, M. Lanzi, C. Rinoldi, S. S. Zargarian, A. Zakrzewska, A. Kosik-Kozioł, P. Nakielski and F. Pierini, *Nanoscale Adv.*, 2024, **6**, 1246–1258.
34 F. Rojas, *ElsevierFS Rojas, CB OjedaAnalytica Chim. acta, 2009•Elsevier*.

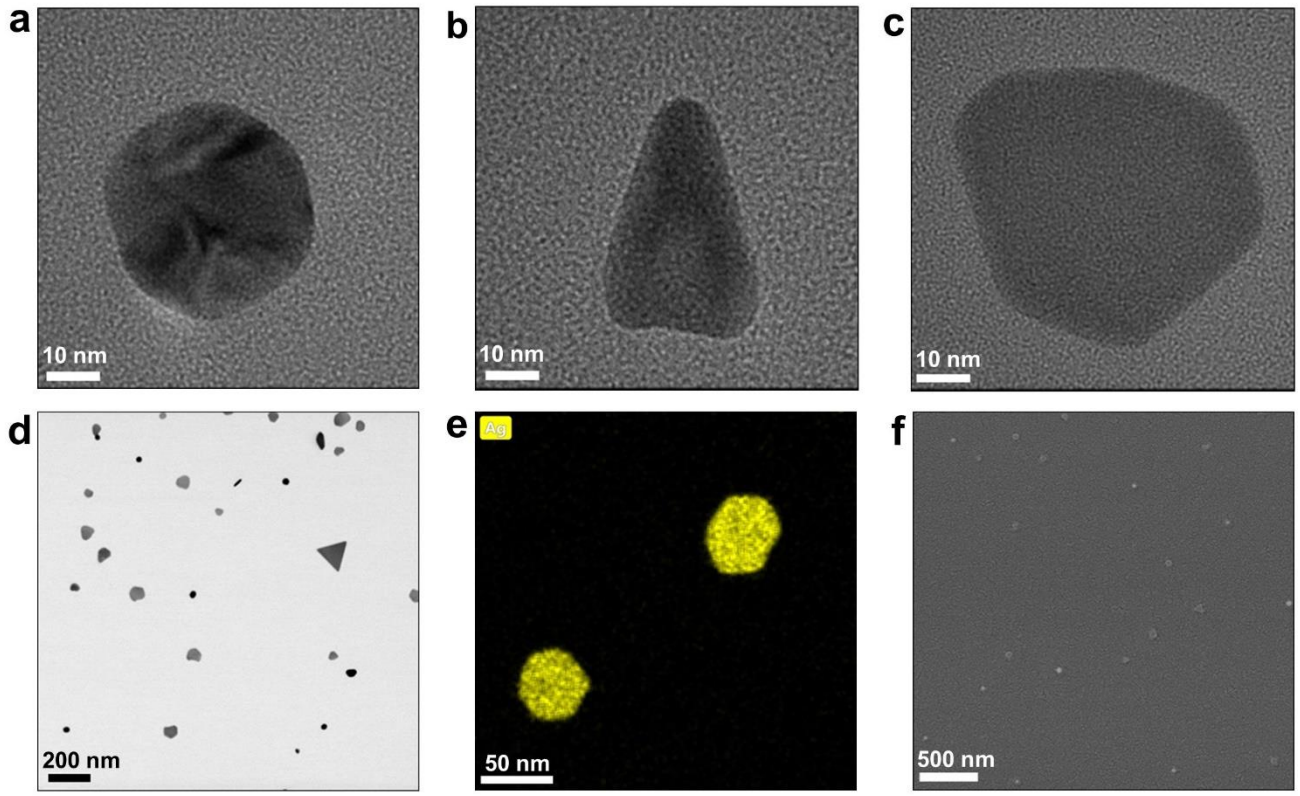

Figure 1. Characterization of silver nanoplates. a-c) TEM images of the AgNPls show the different shapes of the particles, consisting of circular, triangle, and polygonal, with the same average dimension. **d)** TEM image with lower magnification showing the dispersity of the particles, indicating their stability in the system without aggregation. **e)** EDS mapping of the particles showing the average size and distribution of particles. **f)** FE-SEM of the particles, showing their distribution and stability.

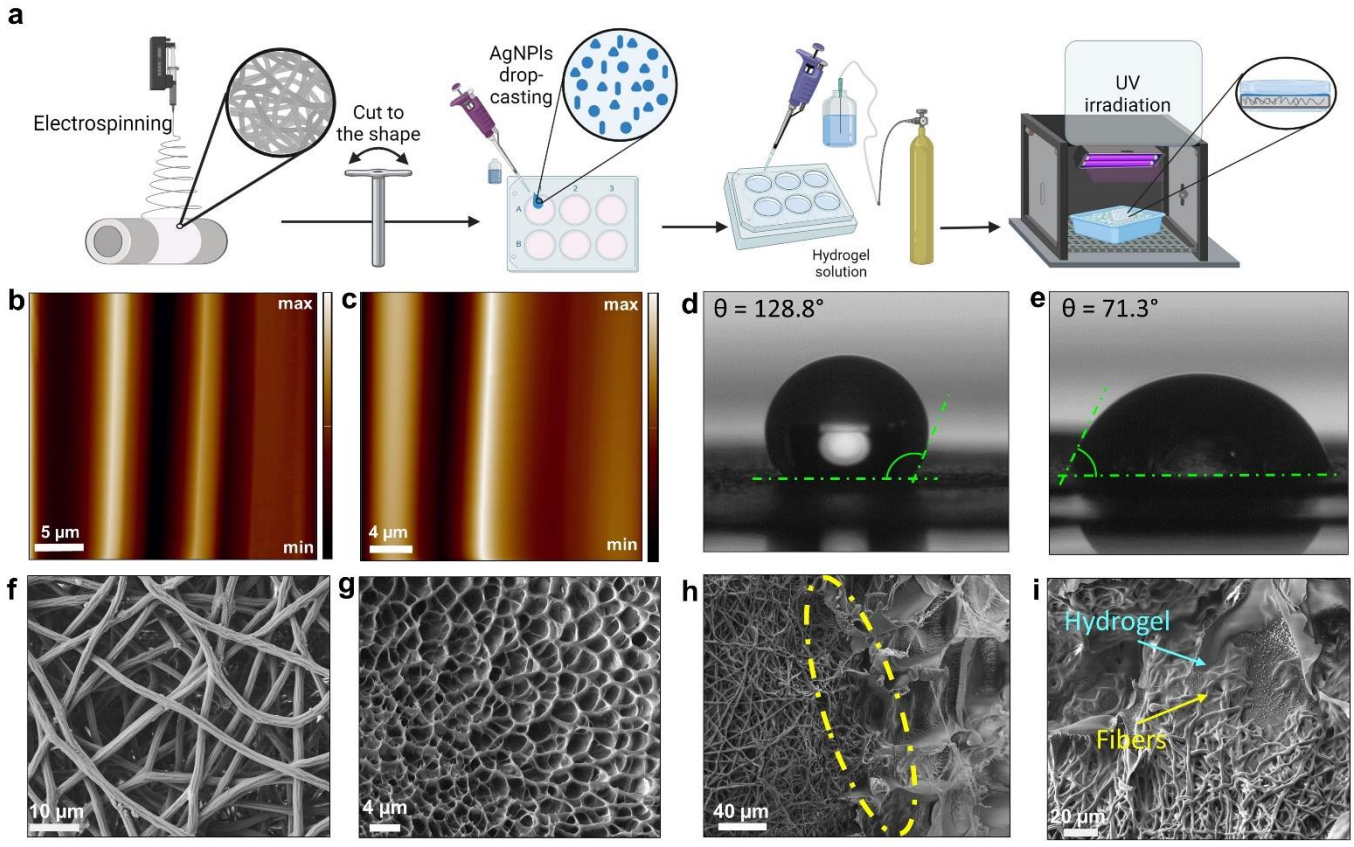

Figure 2. Nanoplatfrom fabrication and characterization. a) Scheme of the fabrication process of the nanoplatforms. The electrospinning process was performed, and the PLCL nanofibers were deposited and cut into the desired shape. AgNPIs were added to each sample, and then hydrogel solution was added to the top of each layer. The whole structure was irradiated under UV light to complete polymerization. **b-c)** AFM images of the PLCL nanofibers before and after applying nanoparticles indicate no changes in the size and shape of the fibers, exhibiting no changes in the surface of nanofibers. **d)** Contact angle of the PLCL fibers before applying the silver particles, demonstrating high hydrophobicity with the contact angle of 129° and **e)** contact angle of PLCL nanofibers after the addition of nanoparticles, which enhanced the hydrophilicity of the fibers, making them more appropriate for layering with hydrogel. **f)** SEM image of PLCL nanofibers presenting their regular defect-free shape, with the average size of 1.478 ± 0.183 µm. **g)** SEM images of the porous NIPAAm-based hydrogel layer with the average pore size of 3.067 ± 0.06 µm. **h-i)** FE-SEM images of the cross-section of the layers, showing the incorporation of the fibers into the hydrogel matrix the stable and robust engagement of the layers, making a steady nanoplatform.

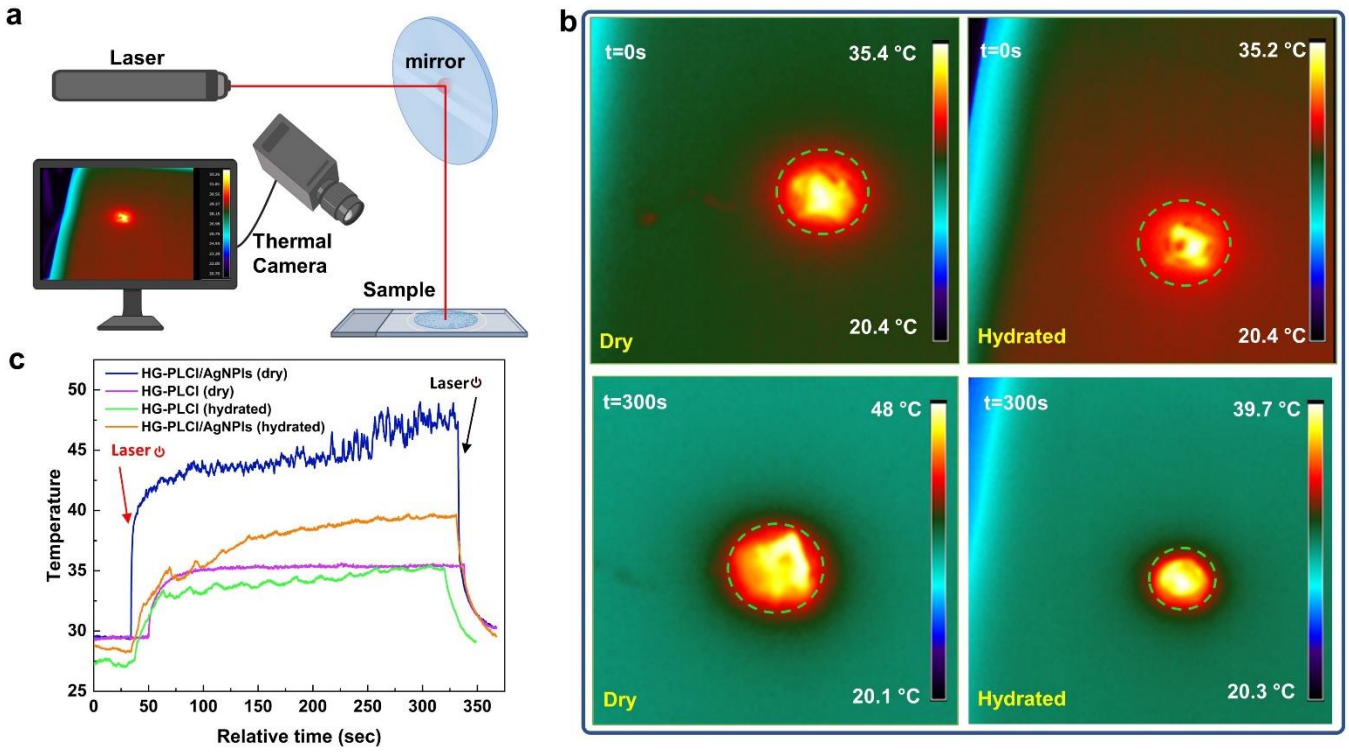

Figure 3. Thermoresponsive properties of the nanoplatforms. a) Schematic of the procedure, using a laser and a thermal camera to evaluate the thermoresponsive properties in terms of heating up and recording the changes in the temperature. **b)** Thermal images of the samples in both dry and hydrated states show the system's temperature rise after 300s. **c)** Temperature vs. time graphs for the platforms with and without AgNPls, demonstrating the fast photothermal responsiveness upon turning on and off the laser.

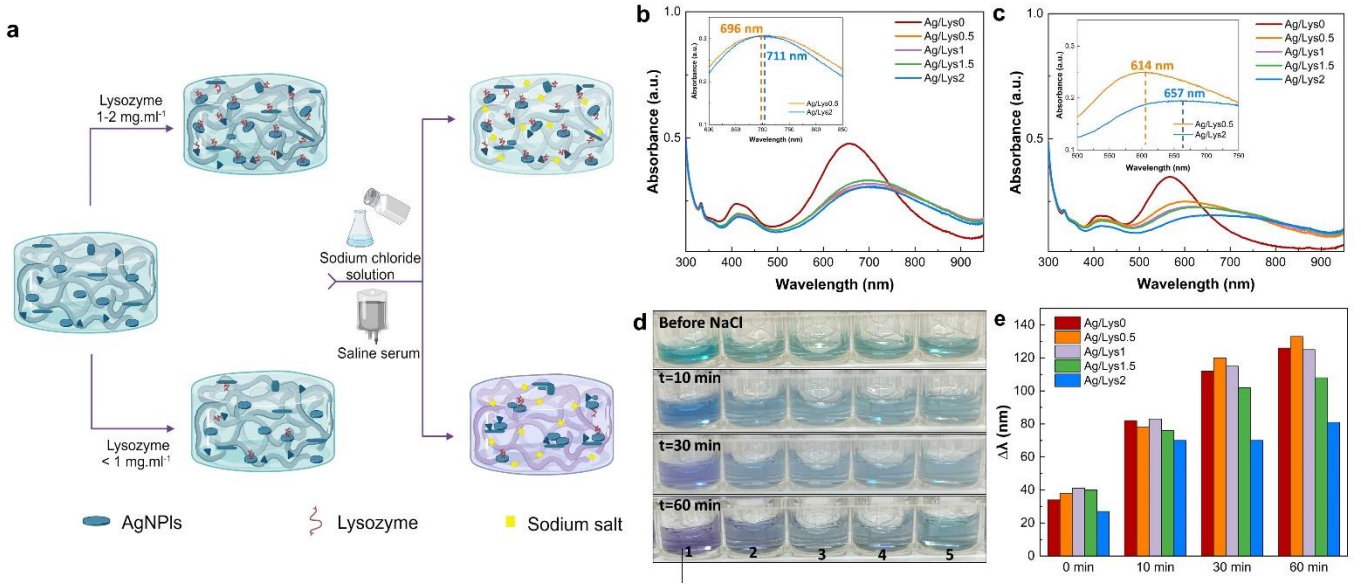

Figure 4. Colorimetry assay. a) Scheme of the procedure explaining the chemistry of colorimetry detection mechanism upon the addition of NaCl salt present in the saline serum. If the amount of lysozyme is not enough in the solution, the upon addition of the salt, a visual color change from blue to purple can be detected in the samples upon aggregation of nanoparticles. **b-c)** Absorbance vs. wavelength of the samples with different amounts of lysozyme before and after adding salt. There are no changes in the peak wavelength before the presence of salt in various concentrations, but after the addition of NaCl, there is a shift of around 75 nm in the peaks of the sample with less than a healthy amount of lysozyme. Under same conditions, the solutions containing more lysozyme in the healthy range, remain with minor changes. **d)** Photographs of the aqueous solutions containing silver nanoplates show the color change of the solutions upon the addition of salt over time. **E)** Δλ is presented with respect to the measured time points. The rate of the changes for each of the samples containing different amounts of lysozyme is is also displayed in the bar chart.

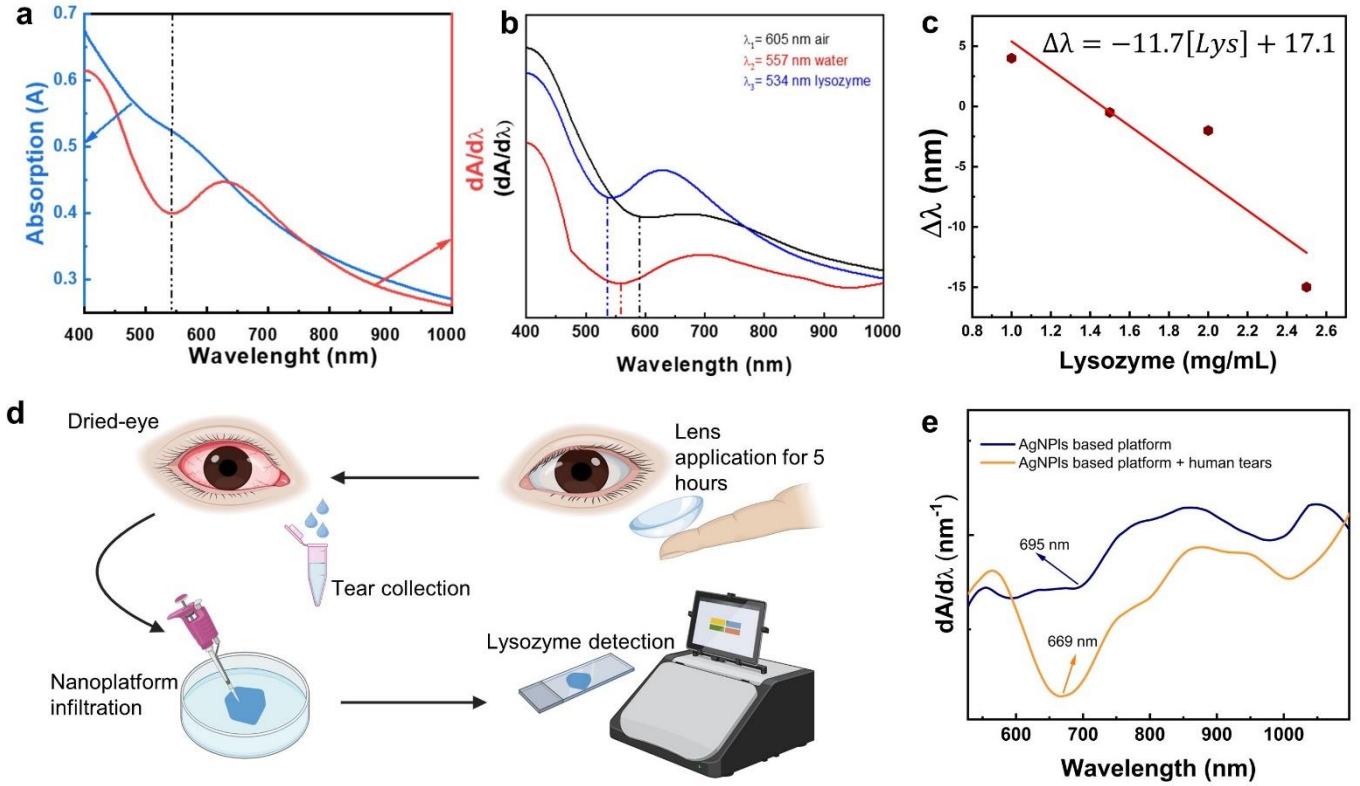

Figure 5. LSPR-based lysozyme biosensing of the nanoplatforms for dry-eye application. a) The absorption spectra of AgNPls-based platform (blue curve) and their first derivative (red curve) show the peak and depth at around 540 nm. **b)** First derivative of the absorption spectra of the AgNPls-based platform reported for different media (air, water and lysozyme). The wavelengths of the depths blue shift as the medium changes from air to water and lysozyme. **c)** Linear correlation between the Δλ and lysozyme concentration. **d)** Schematic of sensing procedure from real human tears, starting with collecting drops from human eyes, and infiltrating the respective nanoplatforms. The amount of lysozyme is detected and calculated using a spectrophotometer. **e)** First derivative of the absorption of an AgNPls- based platform before (blue curve) and after (orange curve) the infiltration with the sample of human tears.